Topological Design of a Trabecular Bone Structure With Morphology and Mechanics Control for Additive Manufacturing

RONG LIU[ID][1,2], (Member, IEEE), YARU CHEN[1], YIN LIU[1], ZIKAI YAN[1], AND YONG-XUAN WANG[2]

[1]Liaoning Key Laboratory of Integrated Circuit and Biomedical Electronic System, School of Biomedical Engineering,
Dalian University of Technology, Dalian 116024, China
[2]School of Information Engineering, Dalian University, Dalian 116001, China

Corresponding author: Yong-Xuan Wang (wangyongxuan@dlu.edu.cn)

ABSTRACT Porous metals are found to be suitable as orthopedic scaffolds. However, only limited control over the internal architecture can be achieved using conventional design methods. The architecture with porosity variation strategy mimicking natural bone is critical to gain favorable combination of mechanical and biological properties for orthopedic implants. In this regard, a topology optimization method with customized morphology and mechanical properties derived from the trabecular bone was proposed to design three-dimensional architectures with gradient porosity resembling the porous structure of bone. In particular, the elastic constants for the trabecular bone were better predicted when the bone volume fraction was supplemented with a three-dimensional structural parameter, i.e., degree of anisotropy. These constants were set as the optimization constrains for morphology control. Then the porous titanium structures were manufactured by selective laser melting technology (SLM). The physical characteristics, mechanical properties of the scaffolds were compared systematically. The experimental results revealed that the as-built samples with the proposed method lead to a good match of morphological accuracy and mechanical properties to that of the bone. It demonstrates that the proposed topology optimization method with controlled morphology and mechanical properties provides an efficient manner for the biomimetic design of orthopedic implants.

INDEX TERMS Additive manufacturing, mechanics control, morphology, topological design, trabecular bone.

I. INTRODUCTION

Skeletal reconstruction of bone defects for load-bearing application is still a major challenge in orthopedic surgery. Solid metals and alloys such as stainless steel and titanium (Ti) have been successfully employed as bone implants owing to their excellent mechanical and bio-logical properties [1]. However, stress-shielding and impermeability have limited their applications [2]. To satisfy the biomechanics requirement of orthopedic scaffolds, a porous structure mimicking natural bone should be taken into consideration.

The associate editor coordinating the review of this manuscript and approving it for publication was Kumaradevan Punithakumar[ID].

Current mainstream direction is to design uniform porous structure constructed by periodically repeating unit cells along all directions [3]. Various topological designs of porous structures by controlling the porosity of implants have been reported [4]. To obtain favorable outcomes, parameters such as porosity, pore size and pore interconnectivity have also been carefully selected. However, the specific selection range of these structural features is still controversial. It is difficult to adjust these parameters to achieve a balance performance. Apparently, conventional regular porous implant design techniques neglect the isotropic pressure micro-environment of the trabecular bone growth and cannot fulfill the biomechanical demands [5]. In essence, the trabecular bone is an

IEEE *Access*

R. Liu *et al.*: Topological Design of a Trabecular Bone Structure With Morphology and Mechanics Control for Additive Manufacturing

anisotropic and porous composite. Therefore, it is imperative to design favorable anisotropic topologies for porous implants.

Conventional fabrication techniques such as gas foaming [6] and freeze drying [7] could lead to irregular trabecular structures and un-controllable interconnectivity, which exhibit a limited control over the internal shape of trabecular structures, resulting in a low repeatability of the morphological and physical properties [8]. Hence, randomly shaped trabecular structures exhibit defects and potential risks with respect to their mechanical and biological properties, such as a reduced stress concentration and fatigue damage [9]. Recently, the selective laser melting (SLM) has been paid much more attention to produce porous structures due to the additive and layer-wise production [10], [11]. It offers a wide range of advantages, including reduction of production steps, a high level of flexibility, a high material use efficiency, and a near net shape production.

Several attempts have been implemented to achieve gradient hierarchical arrangement of pores or random microarchitecture. Typical design strategies include computer aided design (CAD), image-based design, implicit surface modeling and topology optimization [2], [12]–[16]. CAD-based design is obtained by using modern CAD tools which enables the redistribution of the density of structural parts. Surmeneva *et al.* [13] designed triple and double-layered graded porous scaffolds by CAD software. Conventional CAD-based design techniques are inefficient and usually fail to obtain optimal scaffold design because a prohibitively large number of trials would be required in order to achieve a balance performance. Image-based design is based on micro-computed tomography (micro-CT) and image data of original bone. Several studies have examined bone morphology and microarchitecture using micro-CT and designed porous implant using the physical parameters of the trabecular structure such as the porosity and size [17], [18]. Implicit surface modeling of mathematic trigonometric functions is used to maximize the surface volume ratio of the designing scaffold. Dumas *et al.* [14] used MATLAB to generate porosity-graded lattice structures based on a voxelization function. A majority of the porous scaffolds are constructed through the image based reverse modeling method or its combination with the mathematical modeling method to imitate natural bone characteristics. While the aforementioned methods could design structures with controlled and repeatable pore shape or pore size distribution, a vast number of attempts were required and significant difference between designed and as-produced pore morphologies was noticed. The morphology of the scaffold, such as porosity, pore size, and pore interconnectivity, will significantly affect the mechanical properties and biological properties, such as bone ingrowth and the transportation of cells and nutrients. The effects of these factors on scaffold performance are complicated, even conflicting to each other in certain circumstances. It is thus inherently difficult to produce customized porous structures matching closely the envisioned morphological and physical requirements.

Topology optimization, a mathematical method capable of quickly rearranging the materials to attain desired properties while satisfying prescribed multiple objectives and constraints, provides a powerful tool to design scaffolds. However, no related studies regarding how to utilize the information obtained from micro-CT scans and the mechanical performance for porous implant design with topology optimization method have been reported.

The trabecular bone microarchitecture corresponds with the spatial organization and morphology of the trabecular network [19]. The architecture or organization of the trabecular tissue within a specimen contributes to its inherent mechanical properties. Herein, this study focused on topology optimization design to construct customized trabecular structures that closely match the morphological and mechanical requirements of natural bone based on micro-CT stacked images. With the aim to infer on the role of the morphology parameters and mechanical properties to resemble the microstructure of a bone sample, a detailed experimental analysis was carried out by means of micro-CT evaluating all the relevant features to fully characterize the resulting architecture. The representative morphological parameters and mechanical properties were then set as design objectives, and a topological optimization technology was employed using the homo-genization and variable density methods, to reconstruct the trabecular structures.

II. MATERIAL AND METHODS
A. SPECIMEN ANALYSIS USING MICRO-CT SCAN
The specimen of the trabecular bone was obtained from a porcine femoral head of a six-month-old male pig. The porcine trabecular bone was selected because of its similarity to human bones. The study protocol was reviewed and approved by the Review Boards of the Dalian University of Technology, China. The porcine femoral head was scanned and reconstructed into 3D structures using a micro-CT system (Inveon MM Scanners, Siemens Medical Solutions USA, Inc., USA) at the Zhongshan Hospital Affiliated to Dalian University, Dalian, China. The exposure conditions were 80 kV, 500 μA, and a pixel size of 9.41 μm. The data were digitized by a frame grabber and transmitted to a computer for processing with a tomographic reconstruction software (Inveon Acquisition Workplace 1.5, Siemens Medical Solutions USA, Inc.). Projection image data were reconstructed to create 3D images and analyzed using coupled software (Inveon Research Workplace 4.1, Siemens Medical Solutions USA, Inc.). The specimen was made wet prior to the scanning process, to minimize hydration. Owing to the alignment of the trabecular bone in the femoral head along stress trajectories, the trabecular direction in the original 3D image reconstructed using micro-CT scanning was not consistent with the coordinate axis. Therefore, 3D rotation and shear operation were required to ensure that the principal trabecular orientation was aligned with the axis of the specimen. Three corresponding micro-CT images of the representative trabecular bone, with respect to different planes, are shown in Fig. 1.
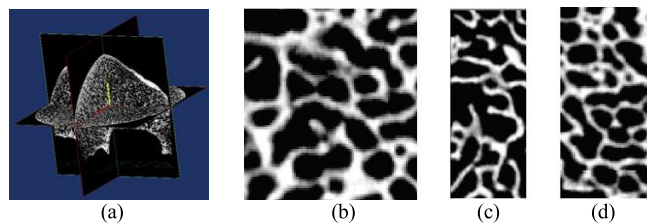
R. Liu *et al.*: Topological Design of a Trabecular Bone Structure With Morphology and Mechanics Control for Additive Manufacturing

IEEE *Access*

FIGURE 1. Corresponding micro-CT images of representative trabecular bone: (a) porcine trabecular bone; (b) coronal plane; (c) transverse plane; and (d) sagittal plane.

The micro-CT images were then stacked in a sequence and inputted to the MIMICS software (MIMICS 10.01, Materialise, Belgium) for image processing, which included pre-processing, threshold segmentation, and region growing.

B. MODELING OF TRABECULAR BONE

According to Wolff's law, the trabecular bone always grows toward the direction of pressure to adapt to the requirements of applied stresses. As a result, there are variations in the mechanical properties, such as the density and structural patterns, in different anatomic regions and orientations. By observing the images of the porcine trabecular microstructure and making several attempts to intercept the structure, it was found that if the femoral head was fit to a sphere, the trabecula in the middle of the maximum radius position was clear and well-connected from the perspective of the coronal plane, which also bearded the effect of external forces. Therefore, the trabecular structure located at the maximum radius of the fitting sphere of the femoral head is intercepted. A stratified and sub-regional reconstruction method was then proposed to divide the intercepted structure into 35 volume elements.

The trabecular architecture was first divided into five layers from the top to bottom (L1–L5), and each layer was then divided into seven 2 mm^3 cubic volume elements. From one side, the volume elements of the first layer were denoted as M1–M7, as for each of the five layers. There were 35 volume elements, as shown in Fig. 2. The images were then compiled to generate a 3D model with a triangular surface mesh for each volume element. Thereafter, the resulting models were refined and smoothed into more manageable mesh densities with undistorted triangular shapes.

C. BONE MORPHOMETRY ANALYSIS

The standard method of the quantitative description of bone architecture is based on the calculation of morphometric indices, which is also referred to as quantitative morphometry [20], [21]. To fully conduct the volumetric measurements, a 3D model reconstruction of the trabecular bone microarchitectures was developed using the micro-CT images. The definition and description of the morphometric indices for the trabecular bone microarchitecture are summarized in Table 1. The basic morphometric indices, which include the measured bone volume (BV), bone surface (BS), and total volume (TV)
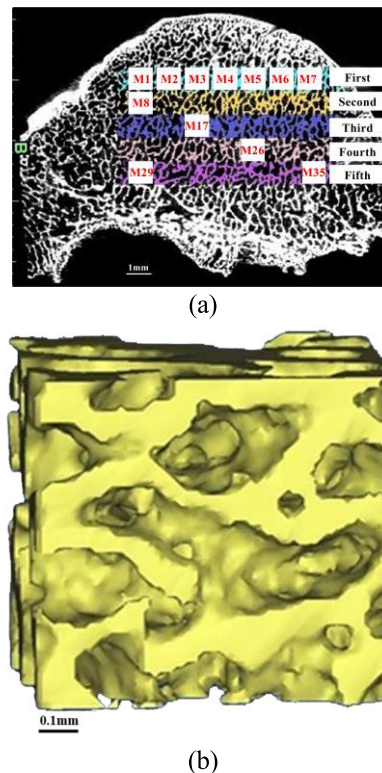

FIGURE 2. Typical reconstructed image of the trabecular bone sample. (a) 35 representative volume elements and associated naming rules of the intercepted trabecular bone; (b) Unit cell structure.

can be directly obtained from the voxels of the 3D models; thus, allowing for the indirect calculation of several indices such as the bone volume fraction (BV/TV), specific bone surface (BS/BV), and bone surface density (BS/TV).

The degree of orientation (DA) of the trabecular bone is expressed by the mean intercept length (MIL) index [20]. The underlying principle of the MIL method is the determination of the number of intersections between a linear grid and a bone interface as a function of the 3-D orientation of the grid v. It indicates the total line length h divided by the number of intersections $c(v)$:

$$DA = h/c(v) \qquad (1)$$

The morphological parameters SMI, Conn and DA were measured using ImageJ software (ImageJ, National Institute of Health, USA) [23]–[25].

D. FINITE ELEMENT MODELING WITH REPRESENTATIVE VOLUME ELEMENT METHOD

After measuring the morphological indices, the mechanical properties of the bone were derived via a finite element analysis. The micromechanical model was set up based on the representative volume element (RVE) technique [26], [27]. The RVE selects a small volume element from the target samples to determine the equivalent physical performance that can be used to represent the characteristics of the overall structure.

TABLE 1. Definition and description of morphometric indices for trabecular bone.

Abbreviation	Parameter	Description	Standard unit
BV	Bone Volume	Volume of the region segmented as bone	mm^3
TV	Total Volume	Volume of the entire region of tissue	mm^3
BV/TV	Volume Fraction	The ratio of bone volume and tissue volume	%
BS	Bone Surface	Surface area of the region segmented as bone	mm^2
BS/BV	Specific Bone Surface	The total area per unit bone volume	1/mm
BS/TV	Bone Surface Density	Ratio of the bone surface to the total volume	1/mm
Tb.Th	Trabecular Thickness	Mean thickness of trabecula	mm
Tb.Sp	Trabecular Separation	Mean distance between trabecula	mm
Tb.N	Trabecular Number	Measure of the average number of trabecula per unit length	1/mm
SMI	Structure Model Index	An indicator of the structure of the trabecula	
Conn	Connectivity	A measure of the degree of connectivity of the trabecula normalized by TV	1/mm^3
DA	Degree of Anisotropy	Length of longest intercept length divided by shortest mean intercept length vector	

The RVE imposes constraints on the model, wherein the displacements along the x-, y-, and z- directions are restricted. Based on the constraints and external load application principle of the RVE method, the nine equivalent properties of the model are solved, i.e., elastic moduli E_x, E_y, and E_z, Poisson ratios v_{xy}, v_{yz}, v_{zx} and shear moduli G_{zx}, G_{yz}, and G_{xy}. The subscript in the elastic moduli symbols stands for the direction, such as E_x is the elastic moduli in -x direction. v_{xy} and G_{xy} is the Poisson ratio and shear moduli calculated from the strain along the x-direction when the external load is applied along the y-direction respectively. Each equivalent property of the RVE can be solved by the finite element mesh model as shown in Fig. 3.
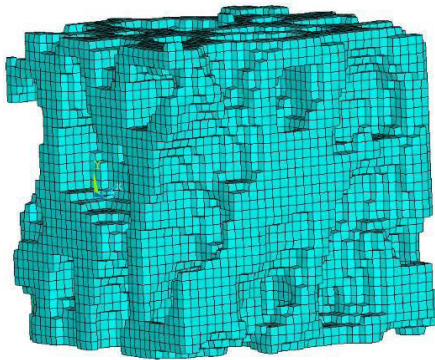

FIGURE 3. Finite element mesh model.

E. TOPOLOGICAL OPTIMIZATION AND RECONSTRUCTION

Topology optimization is commonly used to design complex structures to obtain desirable mechanical performance and physical properties [4], [28]. The variable density method is a point-by-point description in which a void or a solid phase in a local element is represented by an elemental density [29]. In particular, the solid isotropic material with penalization (SIMP) method using this type of description has gained considerable success by converting a structural optimization problem into a material distribution problem [30]. Therefore, we use the SIMP method to design our porous structure in which the interpolation model can be expressed as follows:

$$E_{ijkl}(x) = \rho(x)^p E_{ijkl}^0 \quad p > 1 \quad (2)$$

where E_{ijkl} is the fourth-order elastic modulus tensor for 3D material; $\rho(x)$ is the normalized density function at a certain position x; $\rho(x)^p$ is the power function of density interpolation; p is an adjustable density penalty coefficient to decrease the value of the intermediate density stiffness unit, such that the physical realization of the designed structure can be ensured; E_{ijkl}^0 is the original elastic tensor of the design material.

To calculate the equivalent elastic moduli of the optimized model structure in the iterative process with respect to the mechanical properties and characteristics of the trabecular bone, the homogenization method is used for the topology optimization design [31]. Hence, the objective function is updated in the subsequent optimization design, and a better optimization structure is obtained.

First, the generalized displacement function $\chi_m^{kl}(y)$ is computed by

$$\int_Y (E_{ijkl} - E_{ijmn}\frac{\partial \chi_m^{kl}(y)}{\partial y_n})\frac{\partial v_i}{\partial y_j} dy = 0, \quad \forall \chi_m^{kl}(y) \in V_\Omega \quad (3)$$

where Y is a unit cell domain; v_i represents a continuous function defined in the unit cell; E_{ijkl} and E_{ijmn} are the fourth-order elastic modulus of a material in the unit cell; i, j, k, l, m, and n stand for the coordinate numbers for 3D material; and V_Ω indicates the design domain.

The homogenized elastic modulus of the model E_{ijkl}^H is then calculated as follows:

$$E_{ijkl}^H = \frac{1}{|Y|} \int_Y \left(E_{ijkl} - E_{ijmn}\frac{\partial \chi_m^{kl}(y)}{\partial y_n} \right) dy \quad (4)$$

Subsequently, the design variable of the optimization model, i.e., the cell density ρ_e can be optimized based on the SIMP interpolation model and homogenization method as follows:

$$\begin{aligned}
&find \ \rho_e, \quad e = 1, 2, 3, \cdots, N \\
&\min f(\rho_e) = D_1 \cdot D_2 \\
&\quad D_1 = (E_x - \overline{E_x})^2 + (E_y - \overline{E_y})^2 + (E_z - \overline{E_z})^2 \\
&\quad + (G_{xy} - \overline{G_{xy}})^2 + (G_{yz} - \overline{G_{yz}})^2 + (G_{zx} - \overline{G_{zx}})^2 \\
&\quad + (v_{xy} - \overline{v_{xy}})^2 + (v_{yz} - \overline{v_{yz}})^2 + (v_{zx} - \overline{v_{zx}})^2 \\
&\quad D_2 = \|\mathbf{M}_r - \mathbf{M}_c\|^2 \\
&subject \ to \ V \le V^{upp} \\
&\quad\quad E(x) = \rho(x)^p E^0 \\
&Homogenization \quad\quad\quad\quad\quad\quad\quad\quad\quad\quad (5)
\end{aligned}$$

R. Liu *et al.*: Topological Design of a Trabecular Bone Structure With Morphology and Mechanics Control for Additive Manufacturing

IEEE *Access*

TABLE 2. 3D morphometric parameters derived from micro-CT measurements.

Parameters	L1 (n=7)	L2 (n=7)	L3 (n=7)	L4 (n=7)	L5 (n=7)
BV/TV	0.44±0.05	0.43±0.05	0.42±0.04	0.4±0.03	0.38±0.04
BS/BV (mm^{-1})	14.8±1.53	15.04±1.1	14.95±0.69	14.95±0.6	13.11±1.42
Tb.Th (mm)	0.21±0.02	0.2±0.01	0.2±0.01	0.2±0.02	0.23±0.03
Tb.N (mm^{-1})	1.8±0.03	1.79±0.06	1.71±0.06	1.68±0.1	1.65±0.12
Tb.Sp (mm)	0.35±0.02	0.36±0.03	0.38±0.03	0.39±0.03	0.38±0.03
SMI	2.24±0.59	2.37±0.51	2.38±0.23	2.48±0.21	2.09±0.3
Connectivity	120.05±20.02	124.13±14.98	116.54±18.62	123.61±21.8	110.64±31.13
DA	0.64±0.03	0.67±0.05	0.71±0.04	0.65±0.04	0.67±0.04

Values are presented as mean±standard deviation.

where N is the total number of cells; $f(\rho_e)$ is the objective function; D_1 is the error functions of mechanical properties; D_2 is the error function of morphology indices calculated by weighted norm; $\overline{E_x}, \overline{E_y}, \overline{E_z}, \overline{G_{xy}}, \overline{G_{yz}}, \overline{G_{zx}}, \overline{v_{xy}}, \overline{v_{yz}},$ and $\overline{v_{zx}}$ are the real-time values in the design iteration process; $\mathbf{M}$ is a set of morphology indices listed in Table 1; $\mathbf{M}_r$ is the real-time values in the design iteration process and $\mathbf{M}_c$ is the calculated morphology indices; V^{upp} is the upper limit of the design volume; $E(x) = \rho(x)^p E^0$ is the introduced density interpolation function, the subscript is omitted here; and *Homogenization* is the governing equation in the homogenization method. After setting the unit structure mesh with dimensions of $30 \times 30 \times 30$ and applying a load of 110 GPa (which varied with respect to the materials employed in the experiment), an optimized reconstruction model of the trabecular structure was obtained using an iterative programming procedure which is based on the previously calculated mechanical properties and morphometric indices as the objective function.

III. RESULTS AND DISCUSSIONS

A. MORPHORLOGICAL DATA ANALYSIS

Because the trabecular bone morphology varies across anatomic sites, various parameters were calculated for each volume element of the specimen as summarized in Table 1. Table 2 summarizes the mean and variance of each parameter of each layer. This table indicates that both the BV/TV and trabecular number gradually decreases from L1 to L5. The statistical analysis demonstrates that the BV/TV exhibits statistically significant differences among all layers. The distributions of BV/TV, SMI, connectivity, and DA in each layer are plotted in Fig. 4. The BV/TV, which indicates the amount of bone is in range 33–51%, increased from the edge to the middle within the same layer as shown in Fig. 4(a). This indicates that the overall trend of the volume fraction in different layers of trabeculae is such that the volume fraction is greater when the bone is closer to the upper edge of the femoral head, resulting in a denser distribution of bone trabeculae. In essence, the trabecular bone is a typical biological functional gradient material with density decreasing

conspicuously from the compact exterior region to the cancellous interior region.

The SMI values were found to be mostly distributed within the range of 2–3 (Fig. 4(b)). This indicates that most of the trabecular structures are columnar or a plate–rod mixed structure. The volume elements in the middle of each layer are denser and more plate-like than the ones selected from the two end sites. Consequently, the BV/TV values are higher and the derived SMI values are lower in the middle than around. Because the SMI provides no direct information on connectivity, it should be complemented with a parameter that directly quantifies the connectedness of a 3D structure. This can be achieved by calculating the Euler number shown in Fig. 4(c). There are variations in the connectivity of the lower layer of the femoral head owing to the stress direction of the beam structures and the proximity of the cortical bone to the internal beam structure. Specifically, it is noticed that there are large variation in M7 and M35 at first and fifth layer respectively. This can be assigned to the decreasing in the bone density. Bone density decreases conspicuously from the interior region to exterior region with gradient distribution of porosities along the radial direction. As shown in Figure 4(a), M7 and M35 have the lowest volume fraction. There is a negative correlation between them which will be shown later in Table 3.

The orientation of trabecular structure is another important factor responsible for the anisotropic feature of the bone stress. The orientation and DA estimated by MIL measurements are shown in Fig. 4(d). The figure shows that the internal trabecular anisotropy near the edge of the bone increases with the DA value of the trabecular structure under the influence of the external shape of the femoral head.

These results have demonstrated that the values of micro-CT in bone architecture evaluation revealed substantial variation in architecture according to anatomical location. More importantly, several interesting correlations were identified among the morphologic variables. Correlation analyses were conducted to determine interrelations among parameters. Significance was determined at a p-value of 0.05. The correlations among structural parameters are listed in Table 3.
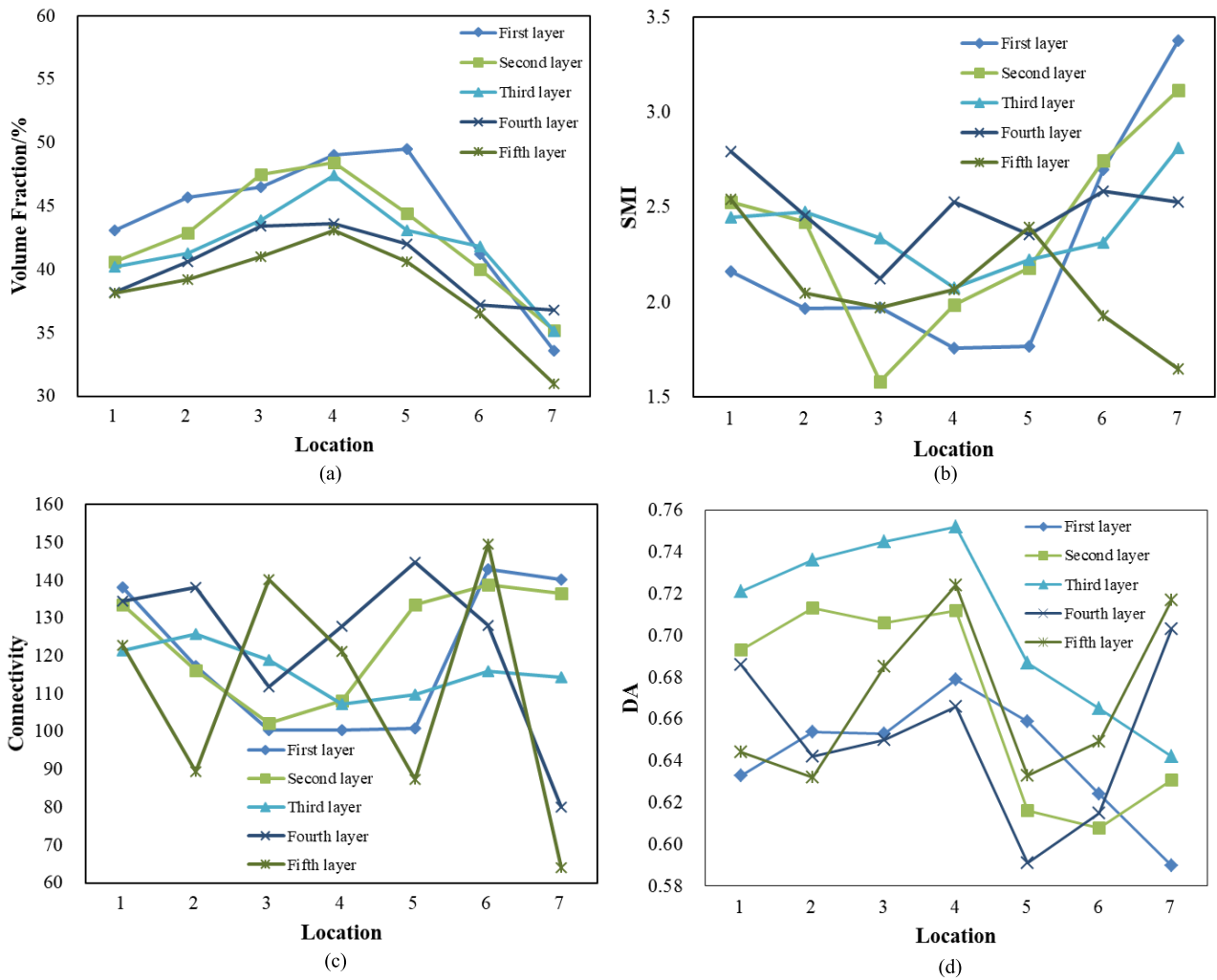
FIGURE 4. Results of morphological parameters: (a) volume fraction distribution; (b) SMI results; (c) connectivity distribution; (d) and DA distribution.

TABLE 3. Correlations among structural parameters.

Parameters		BV/TV	BS/BV	Tb.Th	Tb.N	Tb.Sp	SMI	Connectivity	DA
BV/TV	Correlation	1.000	-0.780*	0.686*	0.226	-0.710	-0.913*	-0.493*	0.433*
	P value		0.000	0.000	0.279	0.070	0.000	0.002	0.040
BS/BV	Correlation		1.000	-0.801*	0.188	0.309*	0.770*	0.510*	-0.349*
	P value			0.000	0.672	0.014	0.000	0.006	0.022
Tb.Th	Correlation			1.000	-0.514*	-0.052	-0.604*	-0.769*	0.276
	P value				0.002	0.765	0.000	0.000	0.109
Tb.N	Correlation				1.000	-0.827*	-0.183	0.540*	-0.003
	P value					0.000	0.293	0.001	0.985
Tb.Sp	Correlation					1.000	0.607*	-0.132	-0.177
	P value						0.000	0.451	0.309
SMI	Correlation						1.000	0.461*	-0.382*
	P value							0.005	0.024
Connectivity	Correlation							1.000	-0.315
	P value								0.065

*means the correlation is significant.

BT/TV is strongly correlated with most of other parameters, such as specific BS, trabecular thickness, SMI, connectivity, and DA. The small value in the volume fraction indicates a loss in the trabecular bone. Therefore, the volume fraction is considered as an objective function of trabecular structures. Tb.Th, Tb.Sp, and Tb.N provide quantitative

R. Liu *et al.*: Topological Design of a Trabecular Bone Structure With Morphology and Mechanics Control for Additive Manufacturing

IEEE *Access*

TABLE 4. Correlations between structural parameters and mechanical properties.

Parameters		Ex	Ey	Ez	Vxy	Vyz	Vzx	Gxy	Gyz	Gzx
BV/TV	*r*	0.687	0.813	0.733	0.118	0.106	0.006	0.712	0.817	0.695
	P	0.000	0.000	0.000	0.500	0.543	0.972	0.000	0.000	0.000
BS/BV	*r*	-0.582	-0.611	-0.653	-0.353	-0.019	0.037	-0.502	-0.618	-0.590
	P	0.000	0.000	0.000	0.037	0.914	0.833	0.002	0.000	0.000
Tb.Th	*r*	0.320	0.320	0.351	0.320	0.056	0.251	0.311	0.319	0.291
	P	0.061	0.061	0.039	0.061	0.748	0.146	0.069	0.062	0.089
Tb.N	*r*	0.356	0.532	0.352	-0.275	0.122	-0.207	0.383	0.534	0.352
	P	0.036	0.001	0.038	0.109	0.485	0.233	0.023	0.001	0.038
Tb.Sp	*r*	-0.630	-0.832	-0.646	0.123	-0.163	0.089	-0.649	-0.836	-0.606
	P	0.000	0.000	0.000	0.480	0.349	0.610	0.000	0.000	0.000
SMI	*r*	-0.561	-0.721	-0.657	-0.177	-0.141	0.114	-0.567	-0.719	-0.627
	P	0.000	0.000	0.000	0.309	0.419	0.514	0.000	0.000	0.000
Connectivity	*r*	-0.255	-0.187	-0.211	-0.118	-0.129	-0.268	-0.346	-0.177	-0.189
	P	0.139	0.281	0.223	0.498	0.460	0.120	0.042	0.310	0.277
DA	*r*	0.148	0.316	0.437	-0.122	-0.030	-0.366	0.187	0.326	0.516
	P	0.397	0.064	0.009	0.484	0.862	0.031	0.282	0.056	0.002

information regarding trabecular microarchitecture. An inverse relationship exists between Th.N and Tb.Sp. While Tb.N differed among five layers, Tb.Th was similar among the five layers.

B. RESULTS OF FINITE ELEMENT ANALYSIS

The mechanical properties in the femur should be studied to design suitable and effective porous implants. Finite element models were constructed and automatically meshed by using ANSYS software (version 15.0; ANSYS, Canonsburg, Pa). With the approach introduced in Section III.E, all nine orthotropic elastic constants of the specimen were predicted. The correlations between structural parameters and mechanical properties are computed and summarized in Table 4. Solely DA is related to the elastic modulus E_x, shear modulus G_{zy}, and Poisson's ratio v_{zx} in the main pressure direction. To predict the primary elastic and shear moduli, the DA plays an important role. Therefore, DA is considered as another objective function of trabecular structures, i.e., all elements in set **M**in Eq. (4) are BV/TV and DA.

C. RECONSTRUCTION UNIT CELL MODELS

Fig. 2 shows that the structures in the third layer (M15–M21) were positioned approximately at the middle of the femoral head, and they were less influenced by the connection between the upper spherical shape and the lower cortical bone. Moreover, there were more significant variations in the morphological parameters and mechanical properties in this layer with less isolated structures. Therefore, the seven structures of the third layer were considered

TABLE 5. Objective functions.

BV/TV	Θ	E (x/y/z)	v	G (x/y/z)
0.40	42.27	3.27/3.29/2.66	0.22/0.24/0.15	1.34/1.33/1.16
0.41	37.81	2.80/3.45/3.02	0.18/0.21/0.16	1.18/1.42/1.30
0.44	33.90	3.07/3.97/3.83	0.21/0.20/0.22	1.35/1.65/1.57
0.47	31.83	4.81/4.90/3.22	0.20/0.22/0.18	2.00/2.00/1.36
0.43	48.70	4.03/4.54/2.94	0.20/0.29/0.26	1.67/1.75/1.16
0.42	39.65	3.57/2.96/1.74	0.25/0.28/0.28	1.43/1.15/0.68
0.35	35.90	2.20/2.36/1.36	0.16/0.29/0.20	0.95/0.92/0.57

as the primary objective functions to construct the cellular structures, as summarized in Table 5.

By considering the volume fraction, DA, and mechanical properties as objective functions, topological optimization by equations (1-5) was used to calculate the density unit distribution of the materials. Moreover, the isolated unit points were filtered using the threshold value and the optimized unit cell models were shown in Fig. 5.

Evidently, the pore structure is anisotropic. Moreover, these structures exhibit excellent pore interconnection both in the in-plane and out-of-plane direction. The reconstructed models exhibited good supportability and low complexities. In addition, the contact surface is sufficiently large to ensure the tightness of the connection. Furthermore, all the directions of the models were connected, thus ensuring a sufficient connectivity of the complex structures. After the porous models were obtained, the equivalent parameters of the mechanical property were calculated. For comparison, the equivalent parameters of the porous models were calculated considering the mechanical properties as the only optimization objective. For the convenience of description, the trabecular bone was
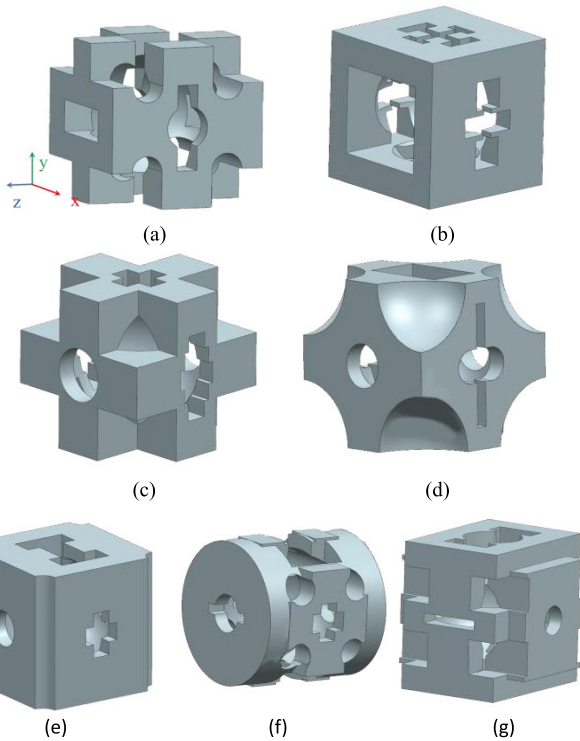
FIGURE 5. Reconstructed unit cell models: (a) M 15; (b) M 16; (c) M 17; (d) M 18; (e) M 19; (f) M 20; and (g) M 21.

TABLE 6. Results of elastic modulus.

	M15	M16	M17	M18	M19	M20	M21
E_{x1}	3.27	3.00	3.37	4.81	4.03	3.57	2.50
E_{x2}	3.57	3.38	3.79	5.34	4.56	3.57	2.87
δ_{Ex1}	9.17	12.67	12.46	11.02	13.15	0.00	14.80
E_{x3}	3.04	3.07	3.67	5.04	4.20	3.36	2.57
δ_{Ex2}	7.03	2.33	8.90	4.78	4.22	5.88	2.80
E_{y1}	3.29	3.45	3.97	4.90	4.54	3.56	2.96
E_{y2}	3.68	3.69	4.22	5.60	4.33	4.00	3.20
δ_{Ey1}	11.85	6.96	6.30	14.29	4.63	12.36	8.11
E_{y3}	3.13	3.12	4.24	5.29	4.20	3.18	2.70
δ_{Ey2}	4.86	9.57	6.80	7.96	7.49	10.67	8.78
E_{z1}	2.66	3.02	3.83	4.21	2.94	2.38	2.36
E_{z2}	3.02	3.42	3.65	4.81	3.36	2.66	2.47
δ_{Ez1}	13.53	13.25	4.70	14.25	14.29	11.76	4.66
E_{z3}	2.40	3.02	3.56	4.37	2.77	2.42	2.16
δ_{Ez2}	9.77	0.00	7.05	3.80	5.78	1.68	8.47

E_{**} is the elastic modulus of the three types. No.1#: E_{x1}, E_{y1}, E_{z1}; No.2# E_{x2}, E_{y2}, E_{z2}; No.3# E_{x3}, E_{y3}, E_{z3} . δ_{E**} is the difference between different types. For example, δ_{Ex1} is the elastic modulus difference between the No.1# type and the No.2# type in *x* direction, while δ_{Ey2} is the elastic modulus difference between the No.1# type and the No.3# type in y direction.

TABLE 7. Results of poisson ratios.

	M15	M16	M17	M18	M19	M20	M21
vxy1	0.22	0.18	0.21	0.20	0.20	0.25	0.16
vxy2	0.26	0.24	0.26	0.21	0.26	0.29	0.19
vxy3	0.24	0.21	0.27	0.16	0.19	0.23	0.17
vyz1	0.24	0.21	0.20	0.22	0.29	0.28	0.29
vyz2	0.23	0.20	0.18	0.24	0.27	0.18	0.23
vyz3	0.19	0.21	0.26	0.31	0.21	0.29	0.21
vzx1	0.15	0.16	0.22	0.18	0.26	0.28	0.20
vzx2	0.19	0.20	0.24	0.25	0.16	0.22	0.23
vzx3	0.16	0.17	0.24	0.25	0.24	0.29	0.21

v_{xy1}, v_{xy2}, v_{xy3}, v_{yz1}, v_{yz2}, v_{yz3}, v_{zx1}, v_{zx2}, and v_{zx3} are the Passion ratios of the three types: first type v_{xy1}, v_{yz1}, v_{zx1}; second type v_{xy2}, v_{yz2}, v_{zx2}; third type v_{xy3}, v_{yz3}, v_{zx3}.

set as the No. 1# structure; and the porous models with the mechanical properties as the only optimization goal were set as the No. 2# structures. Moreover, the proposed models developed in this study were set as the No. 3# structures. The results of the equivalent mechanical properties and the errors between the three types are listed in Tables 6–8.

The elastic modulus distributions of the two designed porous models were found to be similar to those of the No. 1# structure. The relative difference of the reconstructed porous models (No. 3#) was 10.20%, which was appro-ximately 4.08% lower than those of the porous models considering the mechanical properties as the objective function (No. 2#). This indicates that our method possesses excellent control of mechanical properties.

The results listed in Table 6 reveal that the Poisson ratios of the two reconstruction methods were similar to those of the trabecular bone, and both were within the range of 0.15–0.35. Therefore, the difference of the Poisson ratio of the recon-structed porous model was not calculated. Table 5 indicates that the shear modulus distributions of the two optimization models were also similar to those of the trabecular bone. The average errors in the No. 2# and No. 3# structures along the *x*-, *y*- and *z*- directions were 7.58%, 11.17%, and 10.76% and approximately 4.82%, 4.13%, and 5.55%, respectively. To compare the performance of three type structures, *t*-test was applied to investigate the influence of structures on the mechanical properties. The results are significant with $p < 0.05$, indicating a significant difference between the elastic modulus of the No. 1# structures and that of the No.2#

$(p_{E_x} = 0.018, p_{E_y} = 0.031, p_{E_z} = 0.025)$.No significant differences were observed between the elastic modulus of the No. 3# and No. 1# structure$(p_{E_x} = 0.492, p_{E_y} = 0.362, p_{E_z} = 0.361)$. Regarding the shear modulus, the differences between the No. 2# and No. 1# along the *x*- and *y*-directions were statistically significant $(p_{G_{xy}} = 0.011, p_{G_{yz}} = 0.001)$; however, no significant difference was observed between that along the *z*-direction $(p_{G_{xy}} = 0.057)$. The differences in the shear modulus between No. 3# and No. 1# structures were not statistically significant $(p_{G_{xy}} = 0.530, p_{G_{yz}} = 0.131, p_{G_{zx}} = 0.085)$. The results demonstrate that the elastic constants of cancellous bone can be better predicted by supplementing morphologic parameters in the topological design process.

D. FABRICATION AND CHARACTERIZATION OF POROUS TI6AL4V STRUCTURES

The SLM is a layer-wise material addition technique that allows generating complex 3D parts by selectively melting successive layers of metal power on top of each other, using the thermal energy supplied by a focused and computer con-trolled laser beam. Medical grade Titanium alloys (Ti6Al4V)

R. Liu *et al.*: Topological Design of a Trabecular Bone Structure With Morphology and Mechanics Control for Additive Manufacturing

IEEE*Access*

TABLE 8. Results of shear modulus.

	M15	M16	M17	M18	M19	M20	M21
Gxy1	1.34	1.27	1.39	2.00	1.67	1.43	1.08
Gxy2	1.42	1.36	1.50	2.20	1.81	1.39	1.20
δGxy1	5.97	7.09	7.91	10.00	8.38	2.80	11.11
Gxy3	1.23	1.27	1.45	2.17	1.77	1.36	1.10
δGxy2	8.21	0.00	4.32	8.50	5.99	4.90	1.85
Gyz1	1.33	1.42	1.65	2.00	1.75	1.39	1.15
Gyz2	1.49	1.53	1.79	2.26	1.71	1.69	1.30
δGyz1	12.03	7.75	8.48	13.00	2.29	21.58	13.04
Gyz3	1.32	1.29	1.68	2.01	1.72	1.23	1.11
δGyz2	0.75	9.15	1.82	0.50	1.71	11.51	3.48
Gzx1	1.16	1.30	1.57	1.79	1.16	0.92	0.99
Gzx2	1.27	1.42	1.48	1.92	1.44	1.09	1.00
δGzx1	9.48	9.23	5.73	7.26	24.14	18.48	1.01
Gzx3	1.03	1.29	1.43	1.75	1.12	0.94	0.89
δGzx2	11.21	0.77	8.92	2.23	3.45	2.17	10.10

G_{***} is the shear moduli of the three types: first type G_{xy1}, G_{yz1}, G_{zx1}; second type G_{xy2}, G_{yz2}, G_{zx2}; third type G_{xy3}, G_{yz3}, G_{zx3}. δ_{G***} is the errors between different types. For example, δ_{Gxy1} is the shear moduli errors between the first type and the second type, while δ_{Gyz2} is the shear modulus errors between the first type and the third type.

are widely used as implant material due to their high strength to weight ratio, corrosion resistance, biocompatibility and osseointegration properties. In this study, spherical Ti6Al4V (Extra Low Impurity, ELI) powers (Tekna, ASTM B348, grade 23) were used for fabricating seven porous Ti6Al4V structures by selective laser melting machine (Renishaw AM250, Britain).

The SLM machine was equipped with an ytterbium-doped infrared fiber laser fiber laser with beam spot size 135 μm and a maximum power of 400 W on the powder bed. Micro-CT scans were also performed to determine and validate the fabricated structures' morphology. In addition, according to ISO 13314 [32], compression tests of porous Ti6Al4V (diameter: 10 mm, length: 16 mm, $n = 7$) were performed with a crosshead speed of 1 mm/min (Zwick/Z050, Germany).

The dimensions and pore sizes of the fabricated structures were close to the theoretical values, exhibiting high accuracy and reproducibility. The diameters of the pores in the samples were also similar to those expected from the design. Fig. 6 shows the 3D printing porous titanium structure with unit cell model M20 (as shown in Fig. 5(f)) and its micro-CT images. Both the dimensions and internal structure were reproduced according to the topological optimization design.

The morphological parameters of the fabricated structures were then measured as listed in Table 9. By comparing these results with those of the trabecular bone, the differences in Tb.Th, Tb.N, and Tb.Sp were 5.24%, 4.00%, and 5.70%, respectively. The BS of the designed structures was lower than that of the trabecular bone. Although the cell attachment area was reduced, the structural complexity was reduced and reliability was improved. The trabecular structures were anisotropic in the spatial direction, and the DA error value was 9.20%. Moreover, the structures were symmetrical along
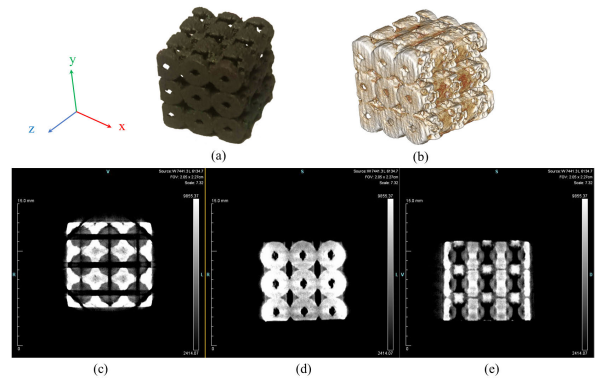

FIGURE 6. The porous titanium structure manufactured by SLM with unit cell model M20. (a) the whole structure; (b) the micro-CT image of the whole structure; (c) the cross-section in the transverse plane; (d) the cross-section in the coronal plane; (e) the cross-section in the sagittal plane.

TABLE 9. Morphological parameters of designed porous structures.

	M15	M16	M17	M18	M19	M20	M21
BS (mm^2)	29.10	33.50	29.46	29.21	31.20	28.56	33.39
BV (mm^3)	3.22	3.35	3.59	3.80	3.46	3.26	2.77
BS/BV	9.04	10.00	8.21	7.69	9.02	8.76	12.05
Tb.Th (mm)	0.18	0.21	0.21	0.21	0.20	0.20	0.21
Tb.N (mm^{-1})	3.70	3.77	3.90	4.16	3.76	3.76	3.75
Tb.Sp (mm)	0.40	0.41	0.38	0.39	0.41	0.41	0.41
Conn	121.00	97.00	106.00	132.00	152.00	100.00	64.00
DA	0.63	0.68	0.69	0.70	0.64	0.60	0.61
SMI	3.31	2.54	2.76	2.67	2.81	3.10	3.11

the x-, y-, and z-directions, thus ensuring the connectivity of the trabecular structures. The connectivity results were within the same variation range as that of the trabecular bone, which indicated that the trabecular structures were well connected. Because SMI was not considered in the optimal design, it exhibited a larger error.

The results revealed that the error between the equivalent mechanical parameters was less than 12%, and the error between the morphological performances was less than 8%. The actual morphological parameters of the porous structures were basically in agreement with the design values, thus confirming the feasibility of the optimization method. As depicted in Table 2 and Table 9, the overall porosity of the cubic volume elements was 58.52%±4.43%, while the as-fabricated samples showed a porosity of about 58.13%±3.75%. The ultimate compressive strength and elastic modulus of the porous Ti6Al4V implants were 81.9±3.8 Mpa and 4.17±0.22 Gpa, which were strong enough for its use as bone implant materials. As reported in Ref. [11], the human cancellous bone has a Yong's modulus range of 0.1-4.5 Gpa and ultimate strength range

of 1.5-38 Mpa. Compared to Ti6Al4V gradient porous structure built by other researches [16], the as-fabricated Ti6Al4V structure presented a satisfying mechanical performance with more reasonable match in modulus and strength as those of the cancellous bone and suitable pore size and overall porosity.

IV. CONCLUSION AND DISCUSSIONS

With the aim to design and fabricate porous structure close resembling the natural bone, the present study investigated the bone structure extensively at the microstructural level from micro-CT scans. The morphological parameters as well as the mechanical properties of the trabecular bone were analyzed qualitatively and quantitatively to develop guidelines for how microstructural data could be applied toclinical implantology.

After analyzing the correlation between morphology para-meters and mechanical properties, BV/TV and DA were identified to be highly related to the structural design. By considering the BV/TV, DA, and mechanical properties as the objective functions, the model was optimized and rebuilt based on the variable density and uniform topological optimization methods. Titanium porous structures designed using the proposed method with a controlled morphology and mechanical control were then fabricated by SLM. The results revealed that the parameters of the reconstruction model were similar to those of the original structure, thus satisfying the initial design requirements, with a considerable reduction in the amount of data required. This study provides new methods to design a porous microarchitecture model that not only satisfy multifunctional requirements but also mimic the trabecular bones, thus permitting us to simulate the complex and anisotropic microstructures of bone tissues.

Some limitations should be acknowledged in this research. It should be underlined that the tests in this study neglect biological experiments. Since internal architecture greatly influences crucial factors for tissue regeneration, such as nutrient diffusion, cell adhesion and matrix deposition, scaffolds have to be carefully designed, keeping in mind mass transport and biological requirements. Even if a good agreement anisotropic mechanical properties between structures produced by AM and human bones was observed, long-term biological performance of porous metallic implants designed through our proposed topology optimization technique needs to be rigorously assessed. Another limitation of this study can be attributed to the application of the load to the trabecular bone in finite element analysis is solely the vertical direction. Hence, the results did not fully reflect the actual case, although they reflected the overall trend of the mechanical properties of the trabecular bone. Moreover, the trabecular structures were designed without considering the different types of beams and applications. To further improve the mechanical and biological performance of these structures, both post-treatment and surface modification is necessary. Clearly, this is just the starting point of a systematic approach that already provided interesting findings that allow

considering the proposed method for potential tissue engineering applications, being planned as a future development.

REFERENCES

[1] J. H. K. Tan, S. L. Sing, and W. Y. Yeong, "Microstructure modelling for metallic additive manufacturing: A review," *Virtual Phys. Prototyping*, vol. 15, no. 1, pp. 87–105, Oct. 2019, doi: 10.1080/17452759.2019.1677345.

[2] W.-M. Chen, Y. M. Xie, G. Imbalzano, J. Shen, S. Xu, S.-J. Lee, and P. V. S. Lee, "Lattice ti structures with low rigidity but compatible mechanical strength: Design of implant materials for trabecular bone," *Int. J. Precis. Eng. Manuf.*, vol. 17, no. 6, pp. 793–799, Jun. 2016, doi: 10.1007/s12541-016-0097-6.

[3] X. P. Tan, Y. J. Tan, C. S. L. Chow, S. B. Tor, and W. Y. Yeong, "Metallic powder-bed based 3D printing of cellular scaffolds for orthopaedic implants: A state-of-the-art review on manufacturing, topological design, mechanical properties and biocompatibility," *Mater. Sci. Eng., C*, vol. 76, pp. 1328–1343, Jul. 2017, doi: 10.1016/j.msec.2017.02.094.

[4] X. Wang, S. Xu, S. Zhou, W. Xu, M. Leary, P. Choong, M. Qian, M. Brandt, and Y. M. Xie, "Topological design and additive manufacturing of porous metals for bone scaffolds and orthopaedic implants: A review," *Biomaterials*, vol. 83, pp. 127–141, Mar. 2016, doi: 10.1016/j.biomaterials.2016.01.012.

[5] F. Li, J. Li, G. Xu, G. Liu, H. Kou, and L. Zhou, "Fabrication, pore structure and compressive behavior of anisotropic porous titanium for human trabecular bone implant applications," *J. Mech. Behav. Biomed. Mater.*, vol. 46, pp. 104–114, Jun. 2015, doi: 10.1016/j.jmbbm.2015.02.023.

[6] B. Q. Li, F. Yan, and X. Lu, "Effect of microstructure on the tensile property of porous ti produced by powder metallurgy technique," *Mater. Sci. Eng., A*, vol. 534, pp. 43–52, Feb. 2012, doi: 10.1016/j.msea.2011.11.028.

[7] H.-D. Jung, S.-W. Yook, T.-S. Jang, Y. Li, H.-E. Kim, and Y.-H. Koh, "Dynamic freeze casting for the production of porous titanium (Ti) scaffolds," *Mater. Sci. Eng., C*, vol. 33, no. 1, pp. 59–63, Jan. 2013, doi: 10.1016/j.msec.2012.08.004.

[8] J. Li, D. Chen, H. Luan, Y. Zhang, and Y. Fan, "Numerical evaluation and prediction of porous implant design and flow performance," *BioMed Res. Int.*, vol. 2018, pp. 1–13, Jun. 2018, doi: 10.1155/2018/1215021.

[9] W.-M. Chen, Y. M. Xie, G. Imbalzano, J. Shen, S. Xu, S.-J. Lee, and P. V. S. Lee, "Lattice Ti structures with low rigidity but compatible mechanical strength: Design of implant materials for trabecular bone," *Int. J. Precis. Eng. Manuf.*, vol. 17, no. 6, pp. 793–799, Jun. 2016, doi: 10.1007/s12541-016-0097-6.

[10] Y. W. Yang, Y. Cheng, S. Peng, L. Xu, C. He, F. Qi, M. Zhao, and C. Shuai, "Microstructure evolution and texture tailoring of reduced graphene oxide reinforced Zn scaffold," *Bioactive Mater.*, vol. 6, pp. 1203–1241, May 2021, doi: 10.1016/j.bioactmat.2020.10.017.

[11] H. Liang, Y. Yang, D. Xie, L. Li, N. Mao, C. Wang, Z. Tian, Q. Jiang, and L. Shen, "Trabecular-like Ti-6Al-4V scaffolds for orthopedic: Fabrication by selective laser melting and *in vitro* biocompatibility," *J. Mater. Sci. Technol.*, vol. 35, no. 7, pp. 1284–1297, Jul. 2019, doi: 10.1016/j.jmst.2019.01.012.

[12] R. Pecci, S. Baiguera, P. Ioppolo, R. Bedini, and C. Del Gaudio, "3D printed scaffolds with random microarchitecture for bone tissue engineering applications: Manufacturing and characterization," *J. Mech. Behav. Biomed. Mater.*, vol. 103, Mar. 2020, Art. no. 103583, doi: 10.1016/j.jmbbm.2019.103583.

[13] M. A. Surmeneva, R. A. Surmenev, E. A. Chudinova, A. Koptioug, M. S. Tkachev, S. N. Gorodzha, and L.-E. Rännar, "Fabrication of multiple-layered gradient cellular metal scaffold via electron beam melting for segmental bone reconstruction," *Mater. Des.*, vol. 133, pp. 195–204, Nov. 2017, doi: 10.1016/j.matdes.2017.07.059.

[14] M. Dumas, P. Terriault, and V. Brailovski, "Modelling and characterization of a porosity graded lattice structure for additively manufactured biomaterials," *Mater. Des.*, vol. 121, pp. 383–392, May 2017, doi: 10.1016/j.matdes.2017.02.021.

[15] A. Hindy, F. Farahmand, F. Pourdanesh, M. Torshabi, A. H. Al Janabi, M. Rasoulianboroujeni, L. Tayebi, and F. S. Tabatabaei, "Synthesis and characterization of 3D-printed functionally graded porous titanium alloy," *J. Mater. Sci.*, vol. 55, no. 21, pp. 9082–9094, Apr. 2020, doi: 10.1007/s10853-020-04645-z.

R. Liu *et al.*: Topological Design of a Trabecular Bone Structure With Morphology and Mechanics Control for Additive Manufacturing

IEEE*Access*

[16] Y.-Z. Xiong, R.-N. Gao, H. Zhang, L.-L. Dong, J.-T. Li, and X. Li, "Rationally designed functionally graded porous Ti6Al4V scaffolds with high strength and toughness built via selective laser melting for load-bearing orthopedic applications," *J. Mech. Behav. Biomed. Mater.*, vol. 104, Apr. 2020, Art. no. 103673, doi: 10.1016/j.jmbbm.2020.103673.

[17] T. M. Keaveny, E. F. Morgan, G. L. Niebur, and O. C. Yeh, "Biomechanics of trabecular bone," *Annu. Rev. Biomed. Eng.*, vol. 3, no. 1, pp. 307–333, Aug. 2001, doi: 10.1146/annurev.bioeng.3.1.307.

[18] K. Bertl, P. Heimel, M. Rökl-Riegler, L. Hirtler, C. Ulm, and W. Zechner, "MicroCT-based evaluation of the trabecular bone quality of different implant anchorage sites for masticatory rehabilitation of the maxilla," *J. Cranio-Maxillofacial Surg.*, vol. 43, no. 6, pp. 961–968, Jul. 2015, doi: 10.1016/j.jcms.2015.04.008.

[19] O. Akhavan, E. Ghaderi, and M. Shahsavar, "Graphene nanogrids for selective and fast osteogenic differentiation of human mesenchymal stem cells," *Carbon*, vol. 59, pp. 200–211, Aug. 2013, doi: 10.1016/j.carbon.2013.03.010.

[20] D. R. Dias, C. R. Leles, A. C. Batista, C. Lindh, and R. F. Ribeiro-Rotta, "Agreement between histomorphometry and microcomputed tomography to assess bone microarchitecture of dental implant sites," *Clin. Implant Dentistry Rel. Res.*, vol. 17, no. 4, pp. 732–741, Aug. 2015, doi: 10.1111/cid.12176.

[21] J. A. Gasser, P. Ingold, K. Grosios, A. Laib, S. Hämmerle, and B. Koller, "Noninvasive monitoring of changes in structural cancellous bone parameters with a novel prototype micro-CT," *J. Bone Mineral Metabolism*, vol. 23, no. S1, pp. 90–96, Jan. 2005, doi: 10.1007/BF03026331.

[22] R. Moreno, M. Borga, and Ö. Smedby, "Generalizing the mean intercept length tensor for gray-level images," *Med. Phys.*, vol. 39, no. 7, pp. 4599–4621, Jul. 2012, doi: 10.1118/1.4730502.

[23] W. S. Rasband. (2018). Image J, U.S. National Institutes of Health. Bethesda, MD, USA. Accessed: May 2, 2018. [Online]. Available: http://rsb.info.nih.gov/ij,1997

[24] A. Odgaard, "Three-dimensional methods for quantification of cancellous bone architecture," *Bone*, vol. 20, no. 4, pp. 315–328, Apr. 1997, doi: 10.1016/S8756-3282(97)00007-0.

[25] R. Liu, X. L. Guo, Y. K. Zhang, and Y. X. Wang, "A methodological review on morphometric parameters of micro-CT trabecular bone images," *Chin. J Biomed Eng.*, vol. 37, no. 2, pp. 237–246, 2018, doi: 10.3969/j.issn.0258-8021.2018.02.014.

[26] Z. H. Xia, Y. F. Zhang, and F. Ellyin, "A unified periodical boundary conditions for representative volume elements of composites and applications," *Int. J. Solids Struct.*, vol. 40, no. 8, pp. 1907–1921, Apr. 2003, doi: 10.1016/S0020-7683(03)00024-6.

[27] M. Amirmaleki, J. Samei, D. E. Green, I. van Riemsdijk, and L. Stewart, "3D micromechanical modeling of dual phase steels using the representative volume element method," *Mech. Mater.*, vol. 101, pp. 27–39, Oct. 2016, doi: 10.1016/j.mechmat.2016.07.011.

[28] M. R. Dias, J. M. Guedes, C. L. Flanagan, S. J. Hollister, and P. R. Fernandes, "Optimization of scaffold design for bone tissue engineering: A computational and experimental study," *Med. Eng. Phys.*, vol. 36, no. 4, pp. 448–457, Apr. 2014, doi: 10.1016/j.medengphy.2014.02.010.

[29] L. Cheng, P. Zhang, E. Biyikli, J. Bai, J. Robbins, and A. To, "Efficient design optimization of variable-density cellular structures for additive manufacturing: Theory and experimental validation," *Rapid Prototyping J.*, vol. 23, no. 4, pp. 660–677, Jun. 2017, doi: 10.1108/RPJ-04-2016-0069.

[30] D. Tcherniak, "Topology optimization of resonating structures using SIMP method," *Int. J. Numer. Methods Eng.*, vol. 54, no. 11, pp. 1605–1622, Aug. 2002, doi: 10.1002/nme.484.

[31] L. Xia and P. Breitkopf, "Design of materials using topology optimization and energy-based homogenization approach in MATLAB," *Struct. Multidisciplinary Optim.*, vol. 52, no. 6, pp. 1229–1241, Jul. 2015, doi: 10.1007/s00158-015-1294-0.

[32] S. L. Sing, S. Huang, and W. Y. Yeong, "Effect of solution heat treatment on microstructure and mechanical properties of laser powder bed fusion produced cobalt-28chromium-6molybdenum," *Mater. Sci. Eng., A*, vol. 769, Jan. 2020, Art. no. 138511, doi: 10.1016/j.msea.2019.138511.

RONG LIU (Member, IEEE) received the Ph.D. degree in electrical engineering from The Chinese University of Hong Kong, Hong Kong, China.

From 2006 to 2011, she was an Assistant Professor with the Department of Biomedical Engineering, Dalian University of Technology, Dalian, Liaoning, China, where she has been an Associate Professor, since 2011. From 2010 to 2011, she was a Research Scientist with the Neuroengineering Laboratory, Biomedical Engineering Department, School of Medicine, Johns Hopkins University. Her research interests include biomedical signal processing and rehabilitation engineering. She is the author of more than 50 articles and holds eight patents.

YARU CHEN is currently pursuing the master's degree from the Dalian University of Technology, Dalian, Liaoning, China. Her current research interests include biomechanics and neurorehabilitation engineering.

YIN LIU is currently pursuing the master's degree from the Dalian University of Technology, Dalian, Liaoning, China. Her current research interest includes mathematical modeling.

ZIKAI YAN received the B.E. degree in electrical engineering and automation from the China University of Mining and Technology, Xuzhou, Jiangsu, China. He is currently pursuing the master's degree from the Dalian University of Technology, Dalian, Liaoning, China. His current research interest includes biomedical signal processing.

YONG-XUAN WANG received the B.Eng. and Ph.D. degrees from the Dalian University of Technology, Dalian, Liaoning, China.

He is currently a Senior Engineer with the School of Information Engineering, Dalian University, Dalian. His current research interests include biomedical signal processing and 3D printing technique for orthopedic implants.

• • •